This open access document is posted as a preprint in the Beilstein Archives at https://doi.org/10.3762/bxiv.2026.13.v1 and is considered to be an early communication for feedback before peer review. Before citing this document, please check if a final, peer-reviewed version has been published.

This document is not formatted, has not undergone copyediting or typesetting, and may contain errors, unsubstantiated scientific claims or preliminary data.

Preprint Title	Microscopic contributions to the deviation from Amontons friction law
Authors	Suresh Ravisankar, Ravikant Kumar, Antonio Cammarata, Thilo Glatzel and Tomas Polcar
Publication Date	08 Apr. 2026
Article Type	Full Research Paper
Supporting Information File 1	SI.zip; 1.1 MB
ORCID® iDs	Suresh Ravisankar - https://orcid.org/0009-0000-9861-0576; Ravikant Kumar - https://orcid.org/0009-0003-7720-2196; Antonio Cammarata - https://orcid.org/0000-0002-5691-0682

License and Terms: This document is copyright 2026 the Author(s); licensee Beilstein-Institut.

This is an open access work under the terms of the Creative Commons Attribution License (https://creativecommons.org/licenses/by/4.0). Please note that the reuse, redistribution and reproduction in particular requires that the author(s) and source are credited and that individual graphics may be subject to special legal provisions.
The license is subject to the Beilstein Archives terms and conditions: https://www.beilstein-archives.org/xiv/terms.
The definitive version of this work can be found at https://doi.org/10.3762/bxiv.2026.13.v1

Microscopic contributions to the deviation from Amontons friction law

Suresh Ravisankar*[1], Ravikant Kumar*[1], Antonio Cammarata[1], Thilo Glatzel[2] and Tomas Polcar[1]

Address: [1]Department of Control Engineering, Faculty of Electrical Engineering, Czech Technical University in Prague, Technicka 2, 16627 Prague 6, Czech Republic and [2]Department of Physics, University of Basel, 4056 Basel, Switzerland

Email: Suresh Ravisankar - ravissur@fel.cvut.cz; Ravikant Kumar - kumarra2@fel.cvut.cz

* Corresponding author

Abstract

We investigate the nanoscale friction behaviour of MX_2 monolayers (M = Mo, W; X = S, Se) on Au(111) and Ag(111) substrates with a silicon tip using classical molecular dynamics simulations with machine-learning-based force fields. This approach enables an accurate description of tip-surface interactions and friction mechanisms at the atomic scale. We observe a pronounced non-monotonic dependence of the friction force on the applied normal load, indicating a breakdown of Amontons's law at the nanoscale. Analysis of lateral force signals and their spatial Fourier transforms reveals the coexistence of multiple sliding modes, including longitudinal sliding, lateral slip, and zig-zag motions. We show that the overall friction response is governed by the relative contributions of these motions. While the qualitative features of friction are largely substrate-independent, both the magnitude of friction and the balance between sliding modes depend sensitively on the substrate-monolayer combination. In particular, Au/$MoSe_2$/Si exhibits significantly reduced friction due to suppression of lateral slip motion. Our results indicate that the method is broadly applicable for probing nanoscale friction in related heterostructures.

Keywords

density functional theory; deep neural network; fourier transform; machine learning force field; molecular dynamics; nanofriction; nonmonotonic; transition metal dichalcogenides

Introduction

Friction arises whenever two contacting surfaces move relative to each other, leading to energy dissipation and material wear in mechanical systems. Unfortunately, liquid lubricants are ineffective in reducing friction under extreme conditions, such as high normal load, high temperature and ultra-high vacuum [1]. In recent years, two-dimensional layered materials such as graphene, boron nitride and transition metal dichalcogenides (TMDs) have emerged as promising solid lubricants in achieving superlubricity on rough and worn surfaces in engineering applications [2-7]. Among them, TMDs stand out for their layered structure and weak van der Waals bonding between the layers, [8,9] which facilitates interlayer shear, resulting in exceptionally low frictional properties in vacuum. However, the dynamic behaviour of the TMD layers with atomic detail during sliding is subject of continuous study, due to the complex phenomena occurring concurrently in tribological conditions. The most used and simple theoretical model of nanoscale friction is the Prandtl-Tomlinson model [10,11]. However, atomistic observation of lateral slips, dynamic deformation and thermal fluctuations is not well captured by this model; indeed, advanced analysis based on the Fourier Transform of the friction force helps to quantify these lateral movements properties [12,13].

The interaction between TMD layers and metallic substrates, together with the influence of a scanning probe tip, determines the overall nanoscale friction response. The atomically flat nature of metallic substrates helps to suppress out-of-plane fluctuations of the TMD layer, resulting in a more stable sliding interface and more reliable investigation of frictional mechanisms [14]. First-principles based calculations have provided valuable insights into the electronic and structural properties of these interfaces [15,16]; however, their application to large-scale friction simulations is limited due to high computational cost. Compared with first-principles calculations, classical molecular dynamics (MD) is a technique capable of simulating dynamic and kinetic problems such as sliding processes and frictional behavior at larger scale and reduced computational load [17-19]. MD simulations are often employed using empirical interatomic potentials, such as ReaxFF [20,21] and reactive empirical bond-order (REBO) potentials [19,22,23]; nevertheless, the parametrisation of such potentials is challenging and time demanding. Fortunately, with the development of machine learning (ML) in material science, this challenge has been well addressed [24]. Various machine learning force fields (MLFFs) have been developed, including the Gaussian approximation potential (GAP) [25], TensorMol [26], the neuroevolution machine learning potential (NEP) [27], and the deep neural network potential (NNP) [28]. Notably, neural networks possess the unique ability to theoretically represent unknown multidimensional real-valued functions with arbitrary precision by selecting appropriate network models. Recent research demonstrates that the NNP model matches the accuracy of quantum mechanics for both finite and extended systems, showcasing its size extensive nature [29,30]. At present, MLFFs have been successfully applied in diverse materials, including TiO_2 [31], Ga_2O_3 [32] and TMDs [29,33,34], making the NNP with the broadest range of applications and the most promising prospects in current research.

In this work, we study the friction response of MX_2 monolayers (M = Mo, W and X = S, Se) deposited on Au(111) and Ag(111) substrates by means of classical MD simulations at different loads and velocities of a scanning tip, employing MLFFs developed for this purpose. Our Fourier analysis of the friction signal allows us to quantify and characterise the nanoscale contributions to the friction response. In particular, we examine the microscopic phenomena responsible for the breakdown of Amontons's law as reflected in the mean friction force; this results in a nonmonotonic friction–load relationship and contributes to significant uncertainty in the extracted coefficient of friction from a linear fit. Significant contribution to such deviation originates from the tip's lateral motion, which also reduces the average friction force, except in the Au/$MoSe_2$/Si system, as the lateral motion is missing from the force profile.

The article is organized as follows: we describe the computational methods in section Computational Details, while the results of the friction simulations of TMDs on different substrates are presented in section Results and Discussion.

Computational Details

Density functional theory (DFT) based calculations for the structural optimisation of TM/MX_2/Si systems (TM = Au, Ag; M = Mo, W and X = S, Se) are performed using the Vienna ab-initio simulation package (VASP) [35]. The interactions between valence electrons and ionic cores are described using the projector augmented-wave (PAW) method [36]. The generalized gradient approximation (GGA) in the Perdew–Burke–Ernzerhof (PBE) form is employed to treat the exchange-correlation energy [37]. The electronic self-consistent field calculations are converged to within 10^{-8} eV, and the atomic positions are relaxed until the residual forces in each atom are less than 10^{-2} eV/Å. A $7 \times 7 \times 1$ Monkhorst–Pack $\boldsymbol{k}$-point mesh [38] is used for Brillouin zone sampling, and the plane-wave basis set is truncated at a kinetic energy cutoff of 500 eV. To accurately capture long-range dispersion interactions, the Grimme DFT-D3 correction [39] is incorporated to account for van der Waals forces between the layers. The ML potential is trained using the DeepMD-kit package with the DeepPot–SE (Deep Potential-Smooth Edition) model [40,41]. The model includes an embedding network and a fitting network. The sizes of these networks are set to (25, 50, 100) and (240, 240, 240), respectively. The cutoff radius is set to 8.0 Å and the descriptors decay smoothly from 0.5 to 8.0 Å. The initial learning rate is set to 0.001 at the beginning of the training process to achieve a final value of 10^{-8}. The total number of training batches are 10^5 for the training in the initial iterations and the active learning process. To automate the active learning process, the DP-GEN workflow is used [42]. All molecular dynamics simulations are performed using the Large-scale Atomic/Molecular Massively Parallel Simulator (LAMMPS) [43] package through the trained ML potentials. The optimised structure of each system is equilibrated at 300 K for 6 ns with a time step of 1 fs by means of a Nosé-Hoover chain with three thermostats. To construct TM/MX_2/Si interfaces, the TM substrate is cleaved from bulk Au and Ag as reported in Ref. 44 and subsequently optimized within the DFT framework. Next, a TMD monolayer is placed on top of the TM substrate in such a way to minimize the lattice mismatch of the resulting heterostructure. A 30 Å vacuum slab orthogonal to the $\boldsymbol{c}$-direction is added on top of the geometry to prevent any interaction of the periodic replicas along the same direction; the geometry of the heterostructure is then relaxed. During the optimization, the bottom layer of the TM substrate is fixed to better mimic the experimental conditions; finally, a Si (111) tip is placed above the heterostructure and the whole system is relaxed. In this last geometric optimization, the bottom TM layer kept fixed, while the Si tip is constrained to relax only along the $\boldsymbol{c}$-direction. An example of model geometry of the full system is reported in Figure 1.

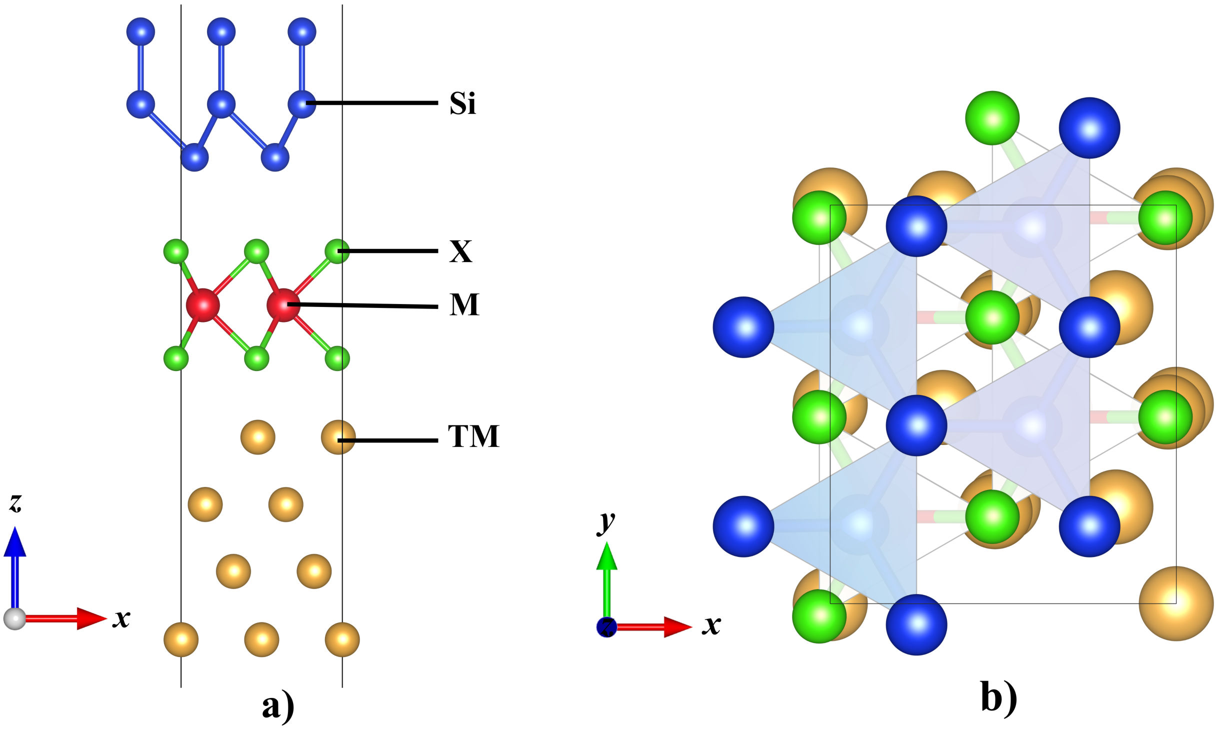

Figure 1: Initial setup to generate strucuture model of TM/MX$_2$/Si. a) Front view and b) top view. The thin black lines indicating the unit cell.

Training of force field

After optimising the full Au/MX$_2$/Si configuration, we proceed to construct the machine-learning force field (MLFF) for the system. Once we obtain the optimised structure, the training data for the MLFF are generated by perturbing the atom positions and cell size by at least 0.01 Å and 0.03 Å, respectively. A total of ~400 configurations are generated to train the MLFF of all the systems and

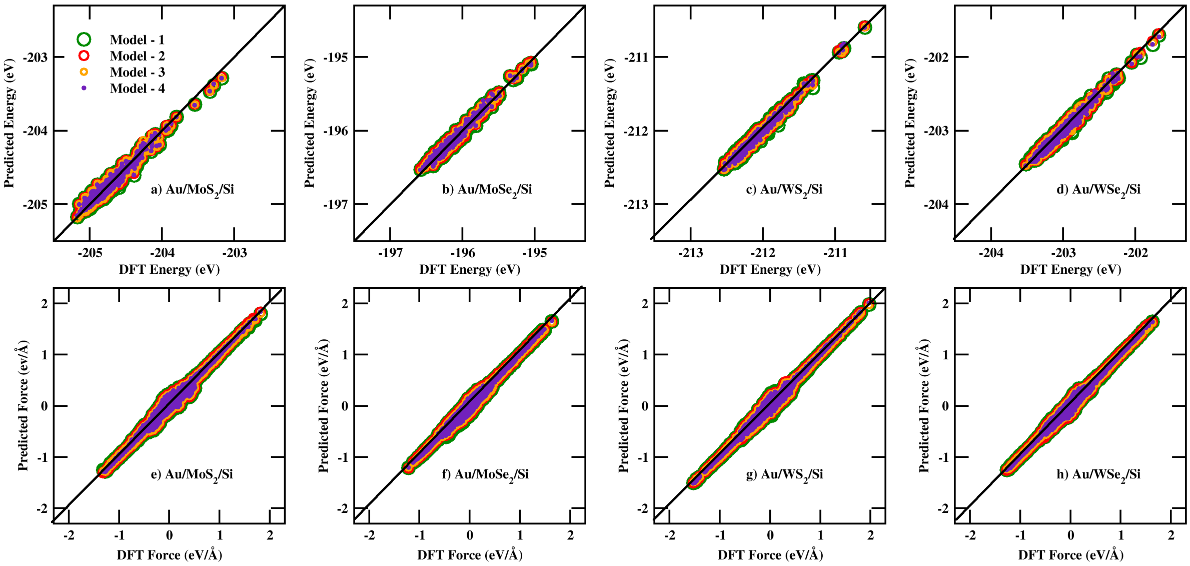

Figure 2: Energy (a–d) and force (e–h) comparisons between predicted and DFT results for Au/MX$_2$/Si systems.

80 configurations are taken for the validation during the active learning process. For all configurations, energy and forces are calculated with the selected DFT setup and a single point calculation, that is at fixed atom geometry and lattice parameters. To effectively improve the MLFF, additional data are generated using an active learning approach as proposed by Zhang et al. [42]. At each iteration, four models are trained using the same input setup but starting with different random seeds. To explore new configurations to enrich the dataset, deep potential molecular dynamics (DPMD) simulations are performed with the initial models as reference, collecting the system's atomic configurations every 10 fs along the trajectories. DPMD simulations are performed for a duration of 500 ps. During the DPMD simulations, the force acting on each atoms in all configurations are evaluated by all four models. The maximum standard deviation of the atomic forces σ_{max} is evaluated as a criterion for the convergence of neural network training

$$\sigma_{\max} = \max{}_i \sqrt{\left\langle \| \boldsymbol{f}_i - \langle \boldsymbol{f}_i \rangle \|^2 \right\rangle} \tag{1}$$

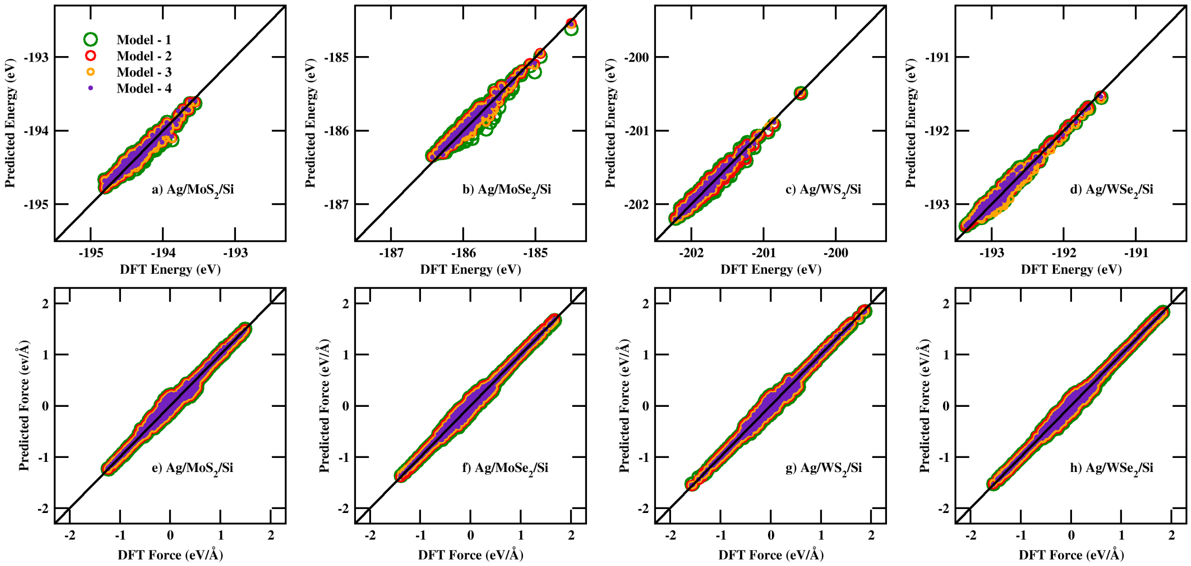

Figure 3: Energy (a–d) and force (e–h) comparisons between predicted and DFT results for Ag/MX$_2$/Si systems.

where $\boldsymbol{f}_i$ is the force acting on i^{th} atom and $\langle \boldsymbol{f}_i \rangle$ is the average value taken from four models. A structure is considered a candidate if the maximum standard deviation falls within the range of $0.05 < \sigma_{max} < 0.15$; while structures with $\sigma_{max} < 0.05$ are considered correct, those with $\sigma_{max} > 0.15$ can be highly distorted configurations and are discarded. The selected structures are then subjected to DFT calculations to obtain the corresponding energies and forces, and included in the dataset. The training with four new models is repeated until the root mean square errors (RMSE) value is reduced. The RMSE values of energy and forces for all the systems are presented in Table 1. All the final models have RMSE of energy and forces ranging from 0.92 to 1.16 meV/atom and 0.019 to 0.021 eV/Å, respectively. This range of RMSE values indicates that the MLFFs model is properly trained with values for the errors typical of surface and interface systems [33,34]. To validate our MLFFs, we optimise the geometry of the heterostructures by using the trained MLFFs; we then compute the RDF scalar products with the DFT optimised structure using the MAISE package [45], in order to check if the two methods yield the same optimised geometry. This analysis shows that the structures optimised with the two methods are almost identical, then confirming the reliability of the MLFFs parametrisation. The same procedure is applied to the case of the Ag substrate.

The predicted energies and forces obtained from the machine-learning force field show very good agreement with the reference DFT results (Figure 2 and Figure 3). This agreement further validates the accuracy of the trained models.

Table 1: The RMSE value of all the trained models.

Monolayer	Substrate	Energy RMSE (meV/atoms)	Force RMSE (eV/Å)	RDF Scalar Product
MoS_2 $MoSe_2$ WS_2 WSe_2	Au	1.5796 1.0288 0.9198 1.1787	0.0213 0.0204 0.0191 0.0193	0.904 0.892 0.946 0.941
MoS_2 $MoSe_2$ WS_2 WSe_2	Ag	1.33 0.941 0.989 1.298	0.0205 0.0196 0.0203 0.0206	0.879 0.878 0.947 0.920

MD Setup for Friction Analysis

For the MD simulations, a 3 × 3 × 1 supercell of the optimised heterostructure was constructed in order to minimise the effects of the system's finite size and to provide a sufficiently large contact area for the sliding process (see Figure 4). The resulting simulation cell contains a total of 360 atoms (See the POSCAR data in Supporting Information File 1, Section I). The bottom layer of the TM substrate is kept fixed throughout the simulation. This constraint prevents artificial translation of the entire system and represents the bulk support typically present in experimental setups; the remaining atoms are allowed to evolve dynamically during the simulation in the NVT ensemble at a temperature equal to 300 K. To model the sliding process, all Si layers are treated as a rigid body to simulate a rigid scanning tip. The tip is moved along the x-direction at constant velocities of 2, 3, 4 and 5 m/s, while there is no constraint on the motion along the y- and z-directions. During sliding, normal loads of 0.0, 0.4, 0.6 and 0.8 nN are applied to the tip along the z-direction. Throughout the simulation, the instantaneous forces acting on the tip and the atomic trajectories are recorded at every 1 fs time step.

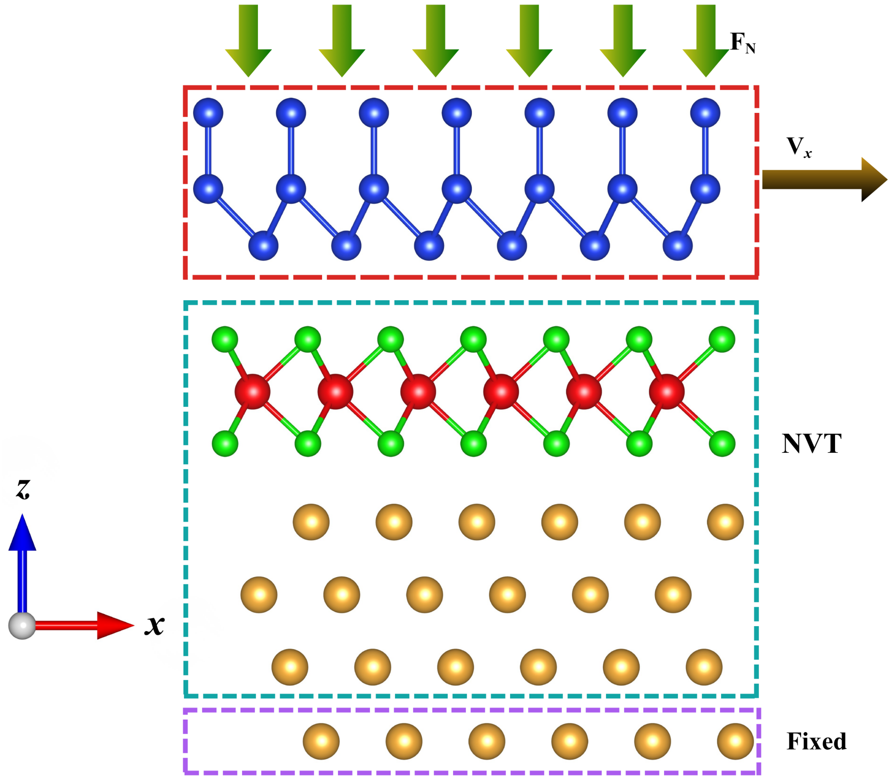

Figure 4: MD simulations setup.

Results and Discussion

Friction Force Analysis

We begin our study of the friction response by considering the friction force profile using 1 ns trajectories under different applied normal loads, as shown in Figure 5. Interestingly, the overall shape of the friction force profile remains nearly identical across all applied loads, indicating negligible load dependence of the profile shape. We then calculate the average friction force acting on the Si tip along the $\boldsymbol{x}$-direction F_{fric}, by averaging over all the snapshots of the trajectory:

$$F_{fric} = -\frac{1}{N_s} \sum_{i=1}^{N_s} \sum_{j=1}^{N_{tip}} F_{xj}(t_i) \tag{2}$$

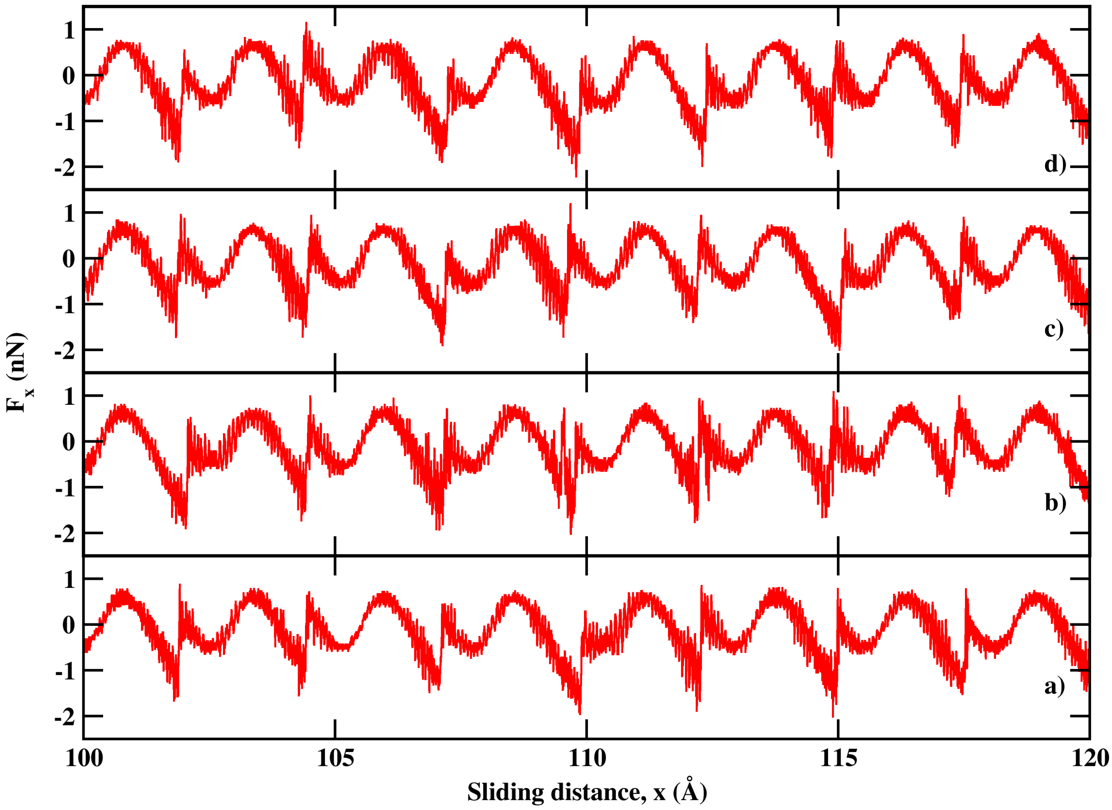

Figure 5: Friction force profile of Au/MoS$_2$/Si with tip moving at 2 m/s for under loads of a) 0 nN, b) 0.4 nN, c) 0.6 nN and d) 0.8 nN.

where N_s is the number of time steps, N_{tip} is the number of atoms in the tip, F_{xj} is the force acting on the j-th atom of the tip at the t_i time step along the sliding $\boldsymbol{x}$-direction, and the negative sign accounts for the fact that friction opposes the direction of motion. The coefficient of friction μ is then calculated according to Amontons's law with the following linearly fitting function:

$$F_{fric} = \mu F_N + F^0_{fric} \tag{3}$$

where F_N is the applied normal load and F^0_{fric} is the friction in the absence of load. The calculated average friction force at varying loads with different velocities for all the systems are reported in Figure 6. Among all systems, Au/WSe$_2$/Si system exhibits the highest friction force across all velocities, followed by Au/MoS$_2$/Si and Au/WS$_2$/Si. Au/MoSe$_2$/Si displays nearly negligible fric-

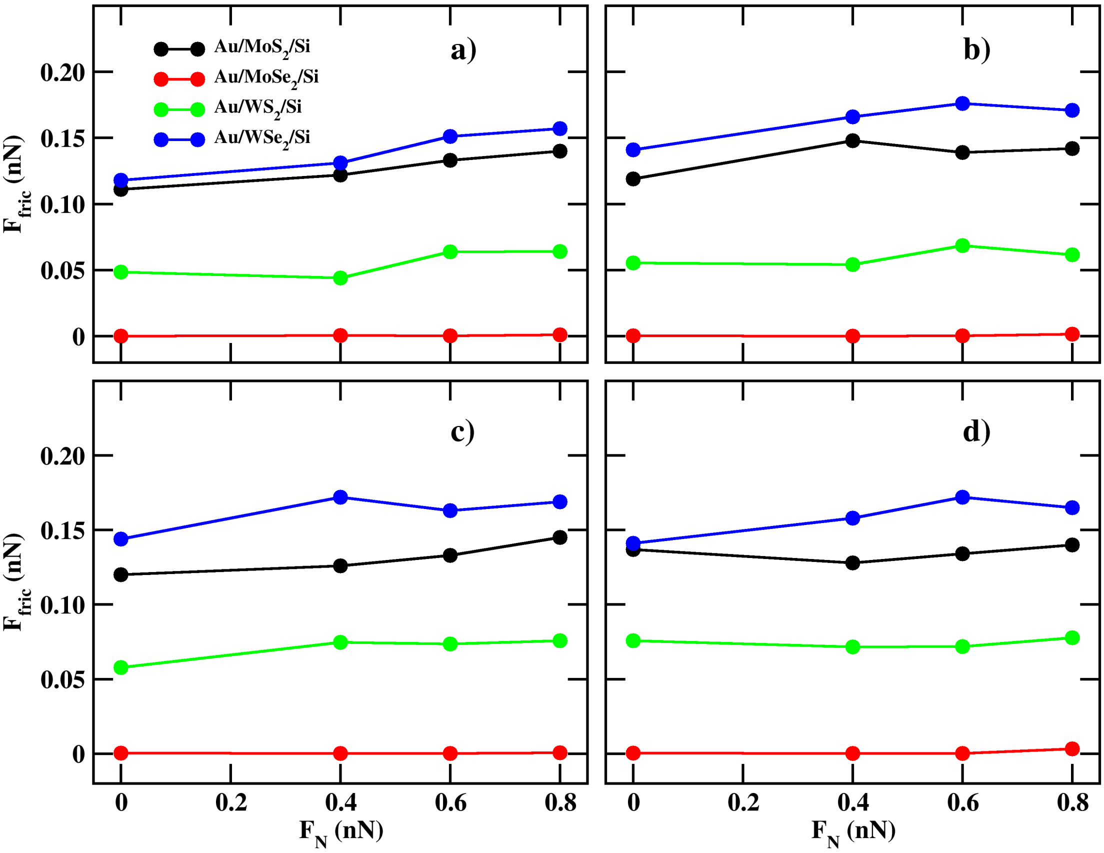

Figure 6: Average friction force as a function of applied load for all systems at tip velocities of (a) 2 m/s, (b) 3 m/s, (c) 4 m/s, and (d) 5 m/s.

tion force across all the applied normal loads. This behaviour is consistent with the corresponding friction force profile, which will be discussed in detail below. In most cases, the friction–load relationship deviates from simple linear behaviour, exhibiting nonmonotonic trends irrespective of the velocities. Looking at Figure 7, which represents the fitted curve corresponding to Figure 6a, the force–fit analysis gives μ values of 0.036, 0.023, 0.051, and 0.0009, with corresponding errors of 0.003, 0.014, 0.009, and 0.0004 for Au/MoS$_2$/Si, Au/WS$_2$/Si, Au/WSe$_2$/Si, and Au/MoSe$_2$/Si, respectively. As a result, the extracted μ shows relatively large errors, indicating that the assumption of a linear friction–load relationship is no longer strictly valid. A similar trend is observed at other velocities (see Supporting Information File 1, Section II, Figure S1, S2 and S3). This behaviour suggests that in our systems, a simple proportional relationship between F_{fric} and F_N cannot fully

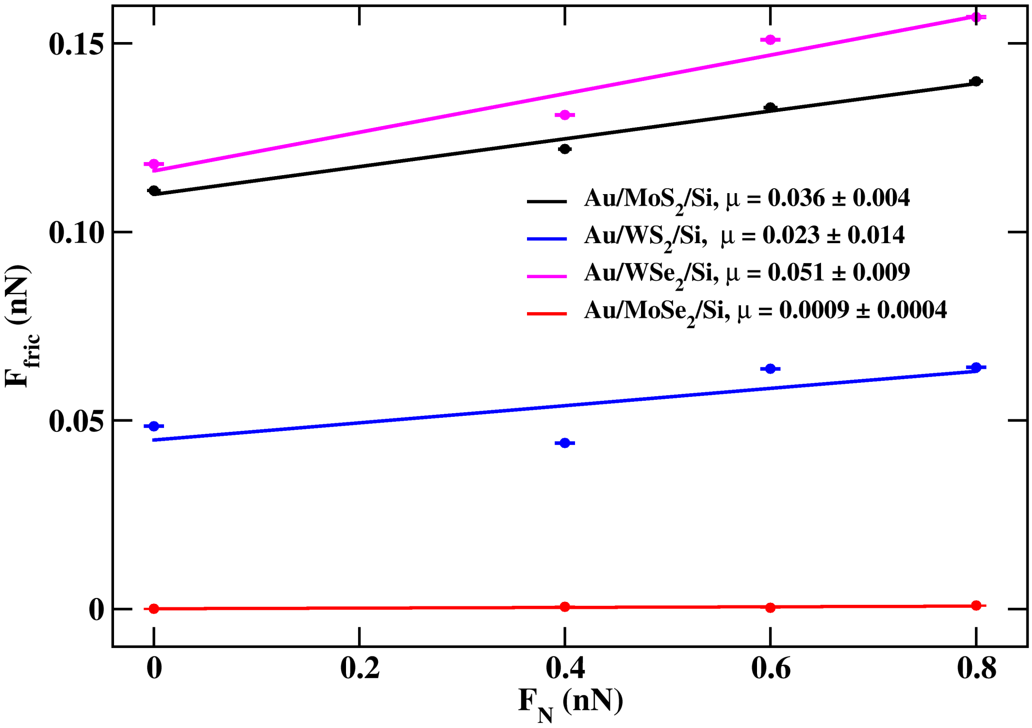

Figure 7: COF obtained from a linear fit of the average friction force as a function of loads for all systems at a tip velocity of 2 m/s.

describe the friction response. This behaviour has already been experimentally observed for an Au/MoS_2/Si monolayer grown on an Au surface [46].

To understand the origin of this nonmonotonic behaviour, we look at the detail of the friction force on the tip during the sliding. Figure 8 shows the friction force on Si tip as a function of the sliding distance for the case of Au/MoS_2/Si system with a velocity of 2 m/s and normal load of 0 nN. Apart from the sliding events along the sliding direction, some extra features can also be observed. Analysis of the geometric sequence along the trajectory reveals that large sudden drops in the lateral force correspond to slip events associated with the primary sliding motion along $\boldsymbol{x}$-direction, named as sliding. In contrast, abrupt increases in the force indicate lateral slip motion involving transverse displacement along $\boldsymbol{y}$-direction, named as lateral slip. Following these events, a gradual

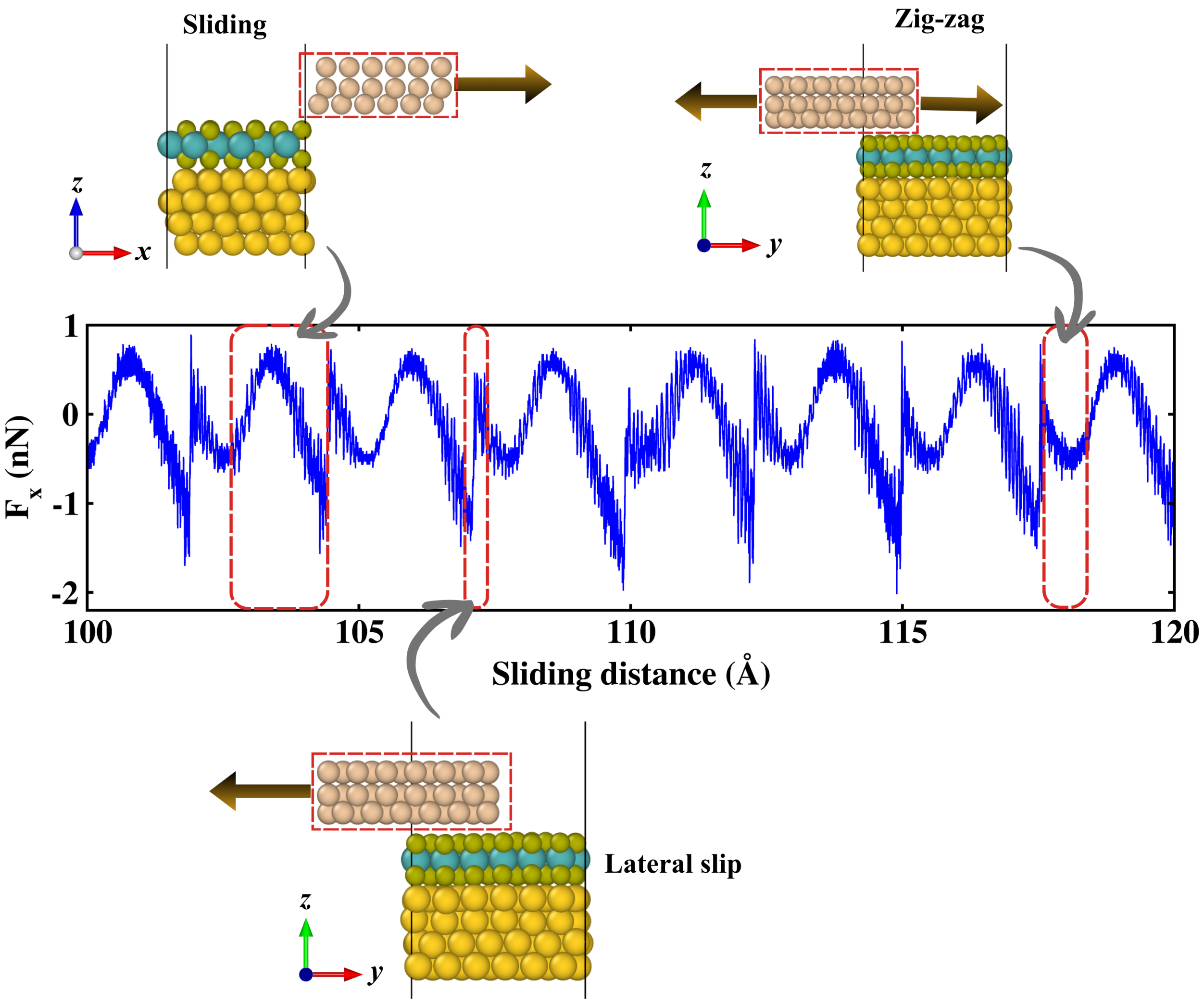

Figure 8: Friction force profile associated with the motion of the tip.

decrease in the force is observed, which corresponds to a zigzag-like motion of the tip as it relaxes while moving laterally along y-direction, named as zig-zag. These observations confirm that the tip does not follow a strictly one-dimensional sliding pathway; instead, the motion involves coupled displacements along both x and y directions, leading to the different frictional behaviour along the x-direction. The zig-zag events indicate that the system explores multiple local minima on the interfacial potential energy surface during sliding; such lateral motion effectively modifies the instantaneous contact configuration and the energy dissipation pathway, leading to fluctuations in the lateral force along x-direction. Interestingly, these features in the force profile occur in most of the cases except the system Au/$MoSe_2$/Si. In the latter cases, the lateral slip and zig-zag part in the force profile is missing which leads to a reduction in the average friction force, as shown in Supporting Information File 1 Figure S4. When two surfaces interact, the surface interactions create a corrugated potential energy landscape that governs the lateral motion during sliding. As the tip moves across this landscape, the motion may not remain strictly confined to the imposed sliding direction; instead, the system can explore neighbouring energy minima, resulting in transverse displacements and complex sliding pathways.

To quantitatively characterise these slip events, we perform a spatial Fourier transform of the forces experienced by the Si tip along the $\boldsymbol{x}$-direction. This analysis provides insight into the nature of the forces that arise from different modes of tip motion, including sliding, lateral motion, and possible nonlinearities in the tip trajectory. Figure 9a displays the spatial Fourier transform of the average force experienced by the tip for the case of Au/MoS$_2$/Si at different normal loads with velocity of 2 m/s. Three magenta dotted lines indicate the main peaks at wave vectors $\boldsymbol{k}_1$, $\boldsymbol{k}_2$ and $\boldsymbol{k}_3$ with the respective intensities I_1, I_2 and I_3. In the Fourier transform, the intensity of a peak is proportional to the number of times the corresponding event occurs, while the inverse of the peak position gives the width of the events on a distance scale. In our simulations, the first peak at $\boldsymbol{k}_1$ corresponds to the sliding process along the $\boldsymbol{x}$-direction, while the second and third peaks (at $\boldsymbol{k}_2$ and $\boldsymbol{k}_3$, respectively) correspond to lateral zig-zag movement and lateral slip along the $\boldsymbol{y}$-direction, respectively. We do not consider other peaks, as their intensity is almost as small as the background noise corresponding to thermal fluctuations of the atomic motions. This is confirmed from the friction force profile where length of the events correlate to the peak positions. The Fourier transform spectra reveal clear correlation between the peak intensities and the average friction force. In particular, the overall ratio I_1/I_2 of the first two peak intensities for all the systems increases as the mean friction force increases (Figure 9b). This trend is observed for all systems across different velocities, except in the case of a Au/MoSe$_2$/Si system; in fact, in this case only a single peak appears in the Fourier transform only at $\boldsymbol{k}_1$, that is, the peak of the sliding, making it impossible to establish a correlation based on the ratio of peak intensities (see Supporting Information File 1, Section II, Figure S5). This trend suggests that when the number of lateral slip events increases, the effective friction force decreases (Figure 9b). Since the friction force is evaluated under different normal loads, the relative contributions of these sliding modes vary with load. As a result, the mean friction force does not exhibit a strictly linear dependence on the applied load, which leads to the nonmonotonic behavior observed in the friction-load relationship, and contributes to the large uncertainty in the extracted coefficient of friction using Amontons's law.

Effect of substrate on friction force

To investigate the effect of the substrate on the lateral friction force, we analyse the trend of the force experienced by the tip as a function of sliding distance under different applied normal loads and different substrates, namely Au and Ag, as shown in Figure 10. We observe that the overall nature of the force signal—particularly the shape of the force profile—remains essentially unchanged as the load increases, provided the monolayer and velocity are kept constant; moreover, in the presence of the Ag substrate, the average force on the tip follows a trend very similar to that observed for the Au substrate. Furthermore, we plot the average friction force as a function of the applied load for all systems and for all sliding velocities, in the presence of the Ag substrate, as shown in Figure 11. We found that the variation of friction force as a function of loads shows nonmonotonic trend and it is consistent with the case of Au substrate that we already have discussed before (see Figure 6). Notably, this behavior is consistently observed for all sliding velocities, indicating that the nonmonotonic features are largely independent of velocity. Overall, among all systems, the Ag/MoS_2/Si system exhibits the highest friction force across all velocities, followed by Ag/WSe_2/Si and Ag/$MoSe_2$/Si, while the Ag/WS_2/Si system shows the lowest friction force over the entire velocity range. In contrast, when considering the Au substrate, the Au/WSe_2/Si system demonstrates the highest friction force at all velocities, followed by Au/MoS_2/Si and Au/WS_2/Si, as discussed in above paragraph. This indicates that the friction force can change significantly depending on the substrate. Furthermore, the calculated μ (as shown in Supporting Information File 1, Section II, Figure S6, S7, S8 and S9) show quite large errors, arising from the nonmonotonic dependence of the friction force on the applied load. We already observed a similar trend in the case of the Au substrate, suggesting that the overall nature of frictional behavior in our systems is largely independent of the substrate. Figure 12 shows the three sharp peaks in FT at velocity 2 m/s for both Ag/MoS$_2$/Si and Au/MoS$_2$/Si systems, which have very similar profiles. We find that the positions of all three peaks remain nearly unchanged for different applied loads and different substrates, indicating that they are independent of loads and substrates. We also observe that the peak positions in the Fourier transforms shift as the monolayer material is varied, confirming that the forces experienced by the tip depend on the specific monolayer (Supporting Information File 1 Section II, Figure S10). In particular, the first peak intensities at varying loads are significantly higher with the Ag/MX$_2$/Si systems compared to the case with Au/MX$_2$/Si systems; this indicates that the friction contribution along the sliding direction is greater when using the Ag substrate (Figure 14a). In contrast, the opposite trend is observed with the Au/WSe$_2$/Si system, where the friction force is higher compared with the Ag/WSe$_2$/Si (Figure 14d). This behaviour correlates with the Fourier transform results (which is shown in Supporting Information File 1, Section II, Figure S10), where the first peak intensity is higher leads to higher in peak intensity ratio (see Figure 13d) in systems with the Au substrate. Overall, these findings suggest that the contribution of multiple sliding and lateral motion in the friction profile strongly influences the average friction force, depending on the specific monolayer and substrate combination.

Focusing to the intensity ratio of both Au/MX$_2$/Si and Ag/MX$_2$/Si system (see Figure 13), the variation of the peak-intensity ratio follows a trend similar to that of the friction force (see Figure 14). In particular, the peak intensity ratios are higher in the case of the Ag substrate compared with the Au substrate, irrespective of the applied loads. Furthermore, the peak-intensity ratio exhibits a clear nonmonotonic dependence on the applied load, consistent with the nonmonotonic behaviour observed in the friction force, resulting in high errors in the estimation of the friction coefficient from a linear fit against the applied load. Therefore, the lateral motion of the tip plays an important role in determining the overall friction force and contributes to both the reduction of the average friction force and the emergence of its nonmonotonic behaviour.

Conclusions

In this study, we investigate the nanoscale friction behaviour of TM/MX_2/Si systems (TM = Au, Ag; M = Mo, W; X = S, Se) using classical molecular dynamics simulations with machine-learning-based force fields trained on DFT data. Our results show that the mean friction force does not follow a strictly linear dependence on the applied normal load. Instead, a nonmonotonic friction–load relationship is observed, which introduces significant uncertainty in determining the coefficient of friction based on Amontons's law. Analysis of the spatial Fourier transform of lateral force signals reveals multiple spectral peaks, with their intensities strongly correlated with the average friction force. The presence of these peaks indicates that the tip motion is not limited to the primary sliding direction but also includes significant lateral contributions. Furthermore, the qualitative features of both the friction force profiles and the Fourier spectra remain similar across different substrates. While the magnitude of friction depends on the specific substrate material, the underlying mechanism responsible for the nonmonotonic behavior—arising from the coupling between longitudinal sliding and lateral motion of the tip—remains essentially substrate-independent. Since our findings demonstrate that frictional forces are influenced by both the monolayer and the underlying substrate, these methods can be effectively employed to investigate nanoscale frictional behaviour in a wide range of heterostructures.

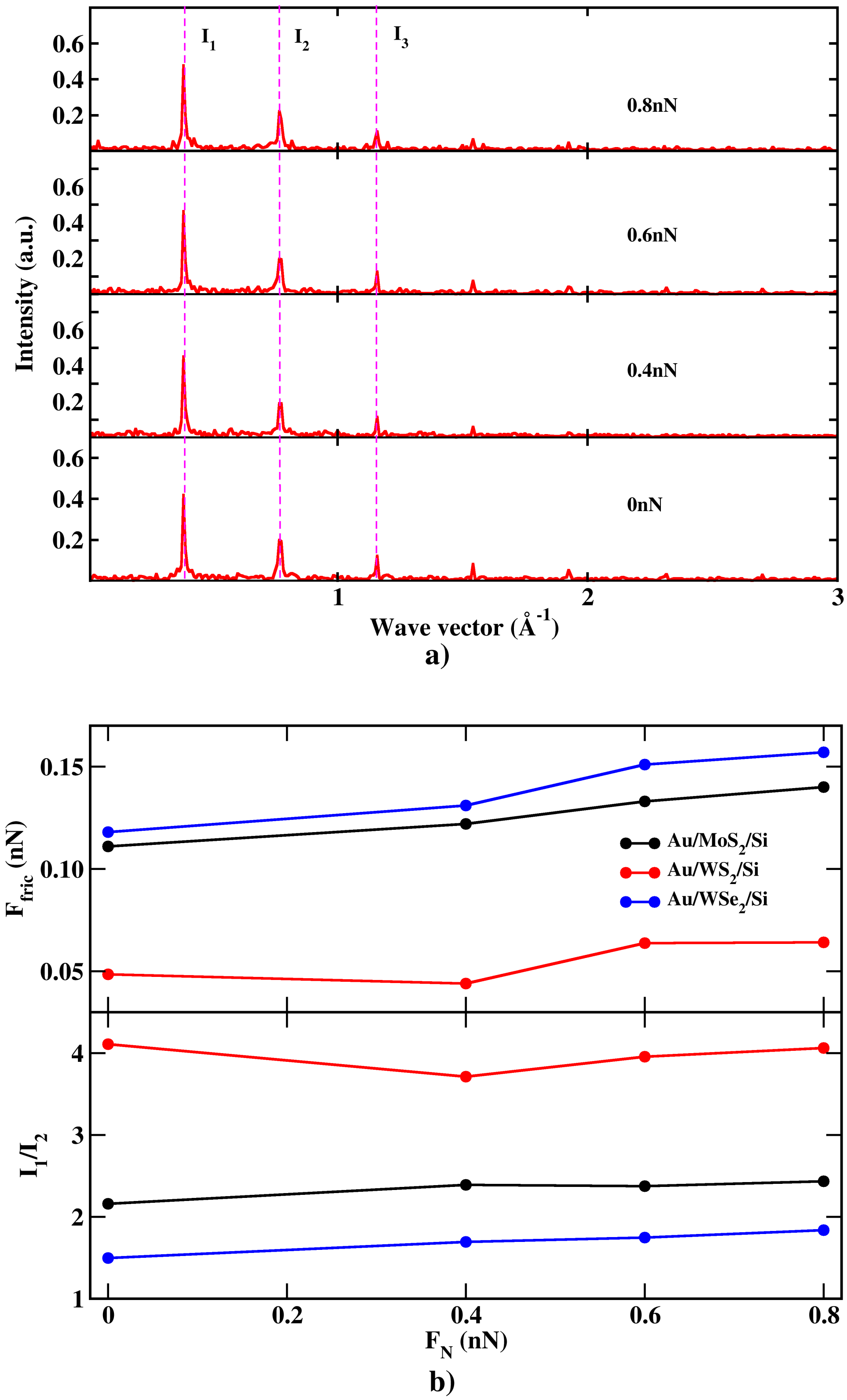

Figure 9: a) Spatial Fourier transform of Au/MoS$_2$/Si with varying loads at velocity 2 m/s, b) Peak intensity ratio and their average friction force with varying loads for all the systems except Au/MoSe$_2$/Si.

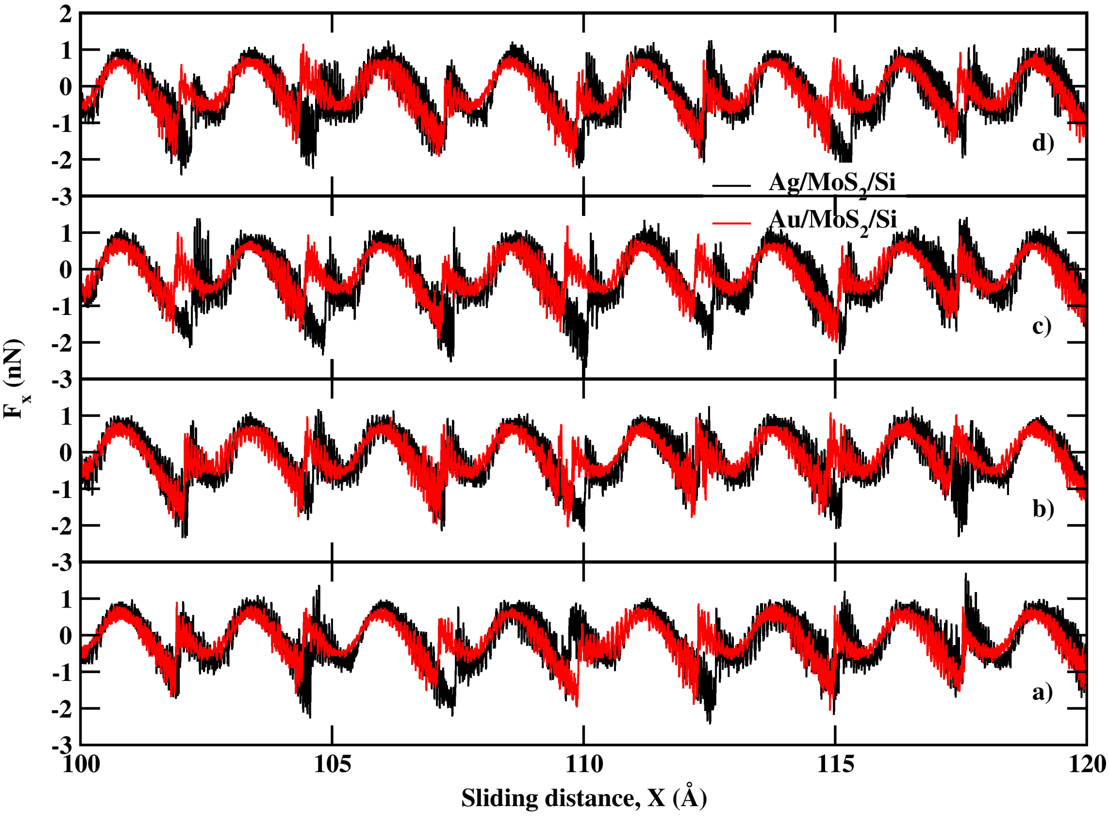

Figure 10: Comparison of friction force profile between Au/MoS_2/Si and Ag/MoS_2/Si as a function of displacement at loads a) 0 nN, b) 0.4 nN, c) 0.6 nN and d) 0.8 nN.

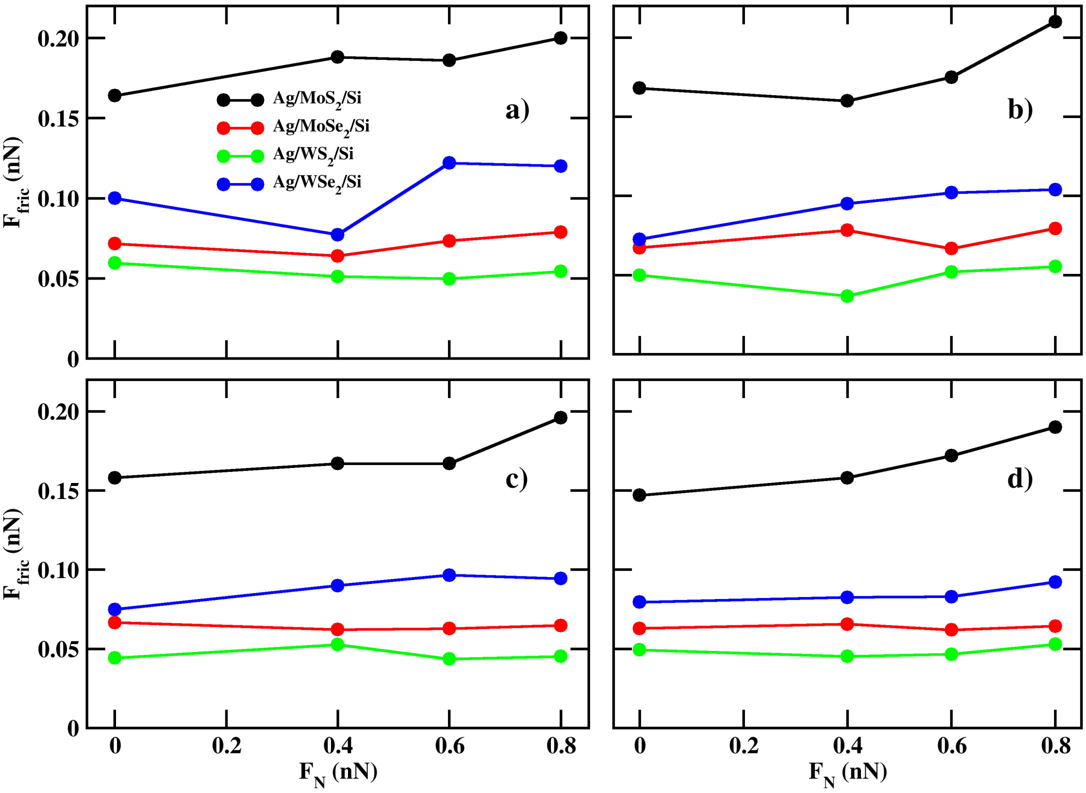

Figure 11: Average friction force as a function of applied loads for all the systems with tip velocities a) 2 m/s, b) 3 m/s, c) 4 m/s d) 5 m/s.

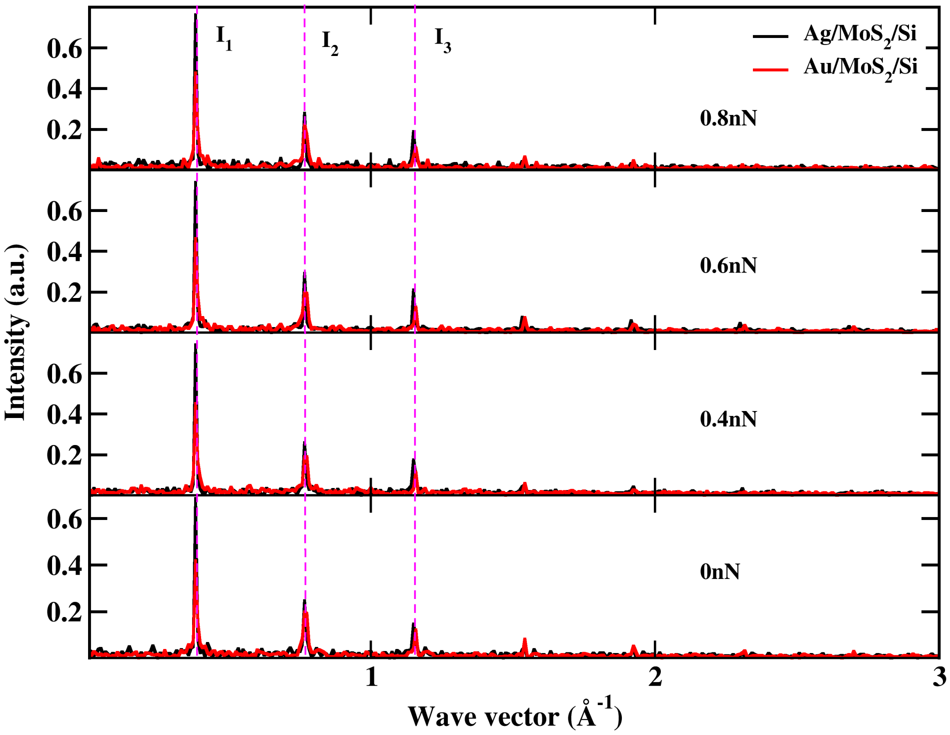

Figure 12: Fourier transform of the force on a tip varying with loads and different substrate for velocity 2 m/s.

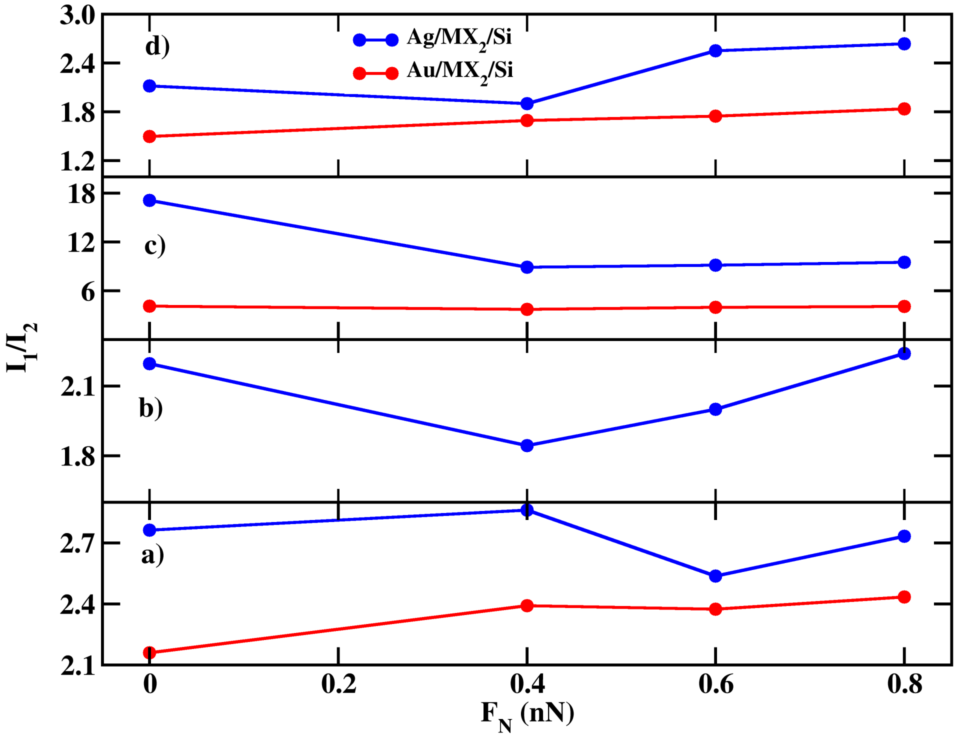

Figure 13: Ratio of the peak intensity I_1 and I_2 varying with loads and different substrate for velocity 2 m/s.

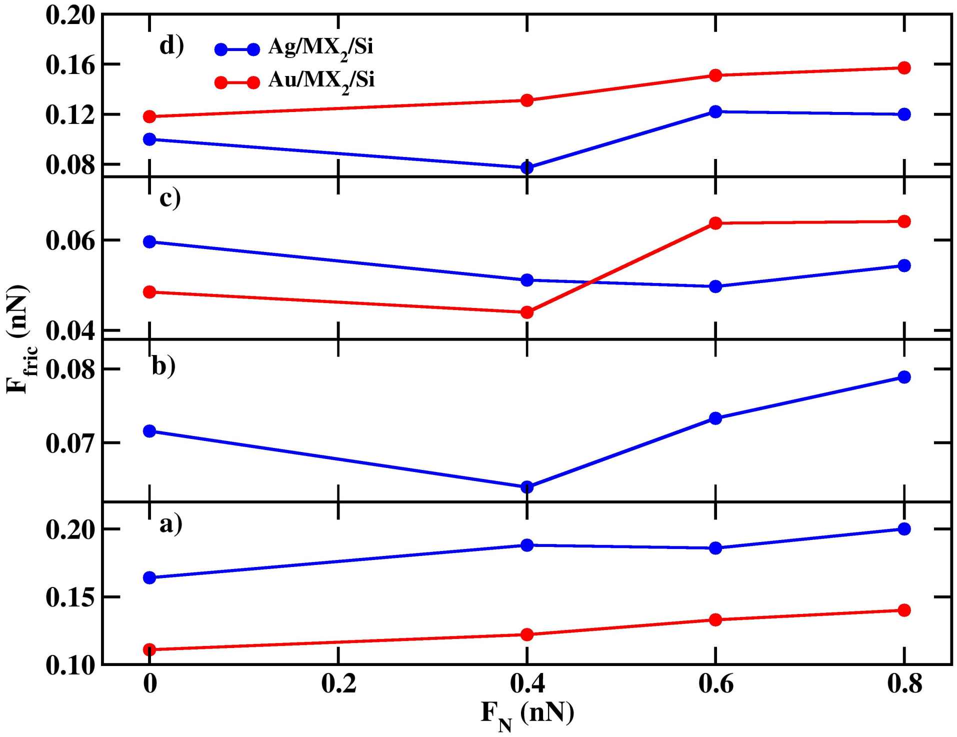

Figure 14: Average friction force, varying with loads and different substrate for velocity 2 m/s.

Supporting Information

Supporting information for Microscopic contributions to the deviation from Amontons friction law.

Supporting Information File 1:

File Name: SI.pdf

File Format: PDF

Title: Additional data and Figures

Acknowledgements

The authors would like to acknowledge the financial support provided by the joint grant 'Nanocontrol' from the Czech Science Foundation (GARC) and the Swiss National Science Foundation (SNSF), with grant numbers 24-12643L and 200021L-219983, respectively. This work was co-funded by the European Union under the project "Robotics and advanced industrial production" (reg. no. CZ.02.01.01/00/22_008/0004590). This work was supported by the Ministry of Education, Youth and Sports of the Czech Republic through the e-INFRA CZ (ID:90254). Use of VESTA software [47] is also acknowledged.

References

1. Sarkar, M.; Mandal, N. *Materials Today: Proceedings* **2022**, *66*, 3762–3768. doi:https://doi.org/10.1016/j.matpr.2022.06.030.

2. Vanossi, A.; Manini, N.; Urbakh, M.; Zapperi, S.; Tosatti, E. *Rev. Mod. Phys.* **2013**, *85*, 529–552. doi:10.1103/RevModPhys.85.529.

3. Zhang, S.; Ma, T.; Erdemir, A.; Li, Q. *Materials Today* **2019**, *26*, 67–86. doi:https://doi.org/10.1016/j.mattod.2018.12.002.

4. Zhang, D.; Li, Z.; Klausen, L. H.; Li, Q.; Dong, M. *Materials Today Physics* **2022**, *27*, 100771. doi:https://doi.org/10.1016/j.mtphys.2022.100771.

5. Marian, M.; Berman, D.; Rota, A.; Jackson, R. L.; Rosenkranz, A. *Advanced Materials Interfaces* **2022**, *9* (3), 2101622. doi:https://doi.org/10.1002/admi.202101622.

6. Wang, J.; Khosravi, A.; Vanossi, A.; Tosatti, E. *Rev. Mod. Phys.* **2024**, *96*, 011002. doi:10.1103/RevModPhys.96.011002.

7. Cammarata, A.; Perviz, E.; Polcar, T. *Progress in Surface Science* **2024**, *99* (3), 100753. doi:https://doi.org/10.1016/j.progsurf.2024.100753.

8. Martin, J. M.; Donnet, C.; Le Mogne, T.; Epicier, T. *Phys. Rev. B* **1993**, *48*, 10583–10586. doi:10.1103/PhysRevB.48.10583.

9. Mukhtar, S. H.; Gulzar, A.; Saleem, S.; Wani, M.; Sehgal, R.; Yakovenko, A.; Goryacheva, I.; Sharma, M. D. *Tribology International* **2024**, *192*, 109194. doi:https://doi.org/10.1016/j.triboint.2023.109194.

10. Prandtl, L. *ZAMM - Journal of Applied Mathematics and Mechanics / Zeitschrift für Angewandte Mathematik und Mechanik* **1928**, *8* (2), 85–106. doi:https://doi.org/10.1002/zamm.19280080202.

11. Tomlinson, G. *The London, Edinburgh, and Dublin Philosophical Magazine and Journal of Science* **1929**, *7* (46), 905–939. doi:10.1080/14786440608564819.

12. Cammarata, A.; Nicolini, P.; Simonovic, K.; Ukraintsev, E.; Polcar, T. *Phys. Rev. B* **2019**, *99*, 094309. doi:10.1103/PhysRevB.99.094309.

13. Bai, H.; Zou, G.; Bao, H.; Li, S.; Ma, F.; Gao, H. *ACS Nano* **2023**, *17* (13), 12594–12602. doi:10.1021/acsnano.3c02915.

14. Lee, C.; Li, Q.; Kalb, W.; Liu, X.-Z.; Berger, H.; Carpick, R. W.; Hone, J. *Science* **2010**, *328* (5974), 76–80. doi:10.1126/science.1184167.

15. Li, Y.; Wu, B.; Ouyang, W.; Liu, Z.; Wang, W. *Nano Letters* **2024**, *24* (4), 1130–1136. doi:10.1021/acs.nanolett.3c03642.

16. Fang, L.; Liu, D.-M.; Guo, Y.; Liao, Z.-M.; Luo, J.-B.; Wen, S.-Z. *Nanotechnology* **2017**, *28* (24), 245703. doi:10.1088/1361-6528/aa712b.

17. Vazirisereshk, M. R.; Hasz, K.; Zhao, M.-Q.; Johnson, A. T. C.; Carpick, R. W.; Martini, A. *ACS Nano* **2020**, *14* (11), 16013–16021. doi:10.1021/acsnano.0c07558.

18. Yao, Y.; Song, Y.; Wu, B.; Scherb, S.; Huang, S.; Hinaut, A.; Glatzel, T.; Meyer, E.; Liu, Z.; Ouyang, W. *Advanced Science* **2025**, *12* (21), 2415884. doi:https://doi.org/10.1002/advs.202415884.

19. Gao, X.; Urbakh, M.; Hod, O. *Phys. Rev. Lett.* **2022**, *129*, 276101. doi:10.1103/PhysRevLett.129.276101.

20. Shi, Y.; Cai, Z.; Pu, J.; Wang, L.; Xue, Q. *Ceramics International* **2019**, *45* (2, Part A), 2258–2265. doi:https://doi.org/10.1016/j.ceramint.2018.10.139.

21. Ostadhossein, A.; Rahnamoun, A.; Wang, Y.; Zhao, P.; Zhang, S.; Crespi, V. H.; van Duin, A. C. T. *The Journal of Physical Chemistry Letters* **2017**, *8* (3), 631–640. doi:10.1021/acs.jpclett.6b02902.

22. Brenner, D. W.; Shenderova, O. A.; Harrison, J. A.; Stuart, S. J.; Ni, B.; Sinnott, S. B. *Journal of Physics: Condensed Matter* **2002**, *14* (4), 783. doi:10.1088/0953-8984/14/4/312.

23. Koczanowski, P.; Nicolini, P.; Khaksar, H.; Gnecco, E. *Small* **2025**, *21* (50), e10186. doi:https://doi.org/10.1002/smll.202510186.

24. Agrawal, A.; Choudhary, A. *APL Materials* **2016**, *4* (5), 053208. doi:10.1063/1.4946894.

25. Bartók, A. P.; Csányi, G. *International Journal of Quantum Chemistry* **2015**, *115* (16), 1051–1057. doi:https://doi.org/10.1002/qua.24927.

26. Yao, K.; Herr, J. E.; Toth, D. W.; Mckintyre, R.; Parkhill, J. *Chem. Sci.* **2018**, *9*, 2261–2269. doi:10.1039/C7SC04934J.

27. Rizzo, T. *Phys. Rev. B* **2021**, *104*, 094203. doi:10.1103/PhysRevB.104.094203.

28. Behler, J.; Parrinello, M. *Phys. Rev. Lett.* **2007**, *98*, 146401. doi:10.1103/PhysRevLett.98.146401.

29. Shaidu, Y.; Naik, M. H.; Louie, S. G.; Neaton, J. B. *npj Computational Materials* **2025**, *11* (1), 273. doi:https://doi.org/10.1038/s41524-025-01761-9.

30. Lu, D.; Wang, H.; Chen, M.; Lin, L.; Car, R.; E, W.; Jia, W.; Zhang, L. *Computer Physics Communications* **2021**, *259*, 107624. doi:https://doi.org/10.1016/j.cpc.2020.107624.

31. Calegari Andrade, M. F.; Selloni, A. *Phys. Rev. Mater.* **2020**, *4*, 113803. doi:10.1103/PhysRevMaterials.4.113803.

32. Li, R.; Liu, Z.; Rohskopf, A.; Gordiz, K.; Henry, A.; Lee, E.; Luo, T. *Applied Physics Letters* **2020**, *117* (15), 152102. doi:10.1063/5.0025051.

33. Liu, X.; Wang, B.; Jia, K.; Wang, Q.; Wang, D.; Xiong, Y. *Journal of Applied Physics* **2024**, *135* (20), 205107. doi:10.1063/5.0201527.

34. Zhou, J.; Fu, Y.; Liu, L.; Liu, C. *The Journal of Physical Chemistry C* **2025**, *129* (13), 6414–6422. doi:10.1021/acs.jpcc.4c08188.

35. Kresse, G.; Furthmüller, J. *Phys. Rev. B* **1996**, *54*, 11169–11186. doi:10.1103/PhysRevB.54.11169.

36. Blöchl, P. E. *Phys. Rev. B* **1994**, *50*, 17953–17979. doi:10.1103/PhysRevB.50.17953.

37. Perdew, J. P.; Burke, K.; Ernzerhof, M. *Phys. Rev. Lett.* **1996**, *77*, 3865–3868. doi:10.1103/PhysRevLett.77.3865.

38. Monkhorst, H. J.; Pack, J. D. *Phys. Rev. B* **1976**, *13*, 5188–5192. doi:10.1103/PhysRevB.13.5188.

39. Grimme, S.; Antony, J.; Ehrlich, S.; Krieg, H. *The Journal of Chemical Physics* **2010**, *132* (15), 154104. doi:10.1063/1.3382344.

40. Zhang, L.; Han, J.; Wang, H.; Car, R.; E, W. *Phys. Rev. Lett.* **2018**, *120*, 143001. doi:10.1103/PhysRevLett.120.143001.

41. Wang, X.; Wang, Y.; Zhang, L.; Dai, F.; Wang, H. *Nucl. Fusion* **2022**, *62*, 126013. doi:10.1088/1741-4326/ac888b.

42. Zhang, Y.; Wang, H.; Chen, W.; Zeng, J.; Zhang, L.; Wang, H.; E, W. *Computer Physics Communications* **2020**, *253*, 107206. doi:https://doi.org/10.1016/j.cpc.2020.107206.

43. Thompson, A. P.; Aktulga, H. M.; Berger, R.; Bolintineanu, D. S.; Brown, W. M.; Crozier, P. S.; in ’t Veld, P. J.; Kohlmeyer, A.; Moore, S. G.; Nguyen, T. D.; Shan, R.; Stevens, M. J.; Tranchida, J.; Trott, C.; Plimpton, S. J. *Computer Physics Communications* **2022**, *271*, 108171. doi:https://doi.org/10.1016/j.cpc.2021.108171.

44. Suh, I.-K.; Ohta, H.; Waseda, Y. *Journal of Materials Science* **1988**, *23* (2), 757–760. doi:https://doi.org/10.1007/BF01174717.

45. Hajinazar, S.; Thorn, A.; Sandoval, E. D.; Kharabadze, S.; Kolmogorov, A. N. *Computer Physics Communications* **2021**, *259*, 107679. doi:https://doi.org/10.1016/j.cpc.2020.107679.

46. Song, Y.; Wang, J.; Hinaut, A.; Scherb, S.; Huang, S.; Glatzel, T.; Tosatti, E.; Meyer, E. *Phys. Rev. Lett.* **2024**, *133*, 136201. doi:10.1103/PhysRevLett.133.136201.

47. Momma, K.; Izumi, F. *Journal of Applied Crystallography* **2008**, *41* (3), 653–658. doi:10.1107/S0021889808012016.